Chinese Physics Letters

LETTER

Possible Inverse Magnetic Melting Effect in vdW-Like Kondo Lattice $CeSn_{0.75}Sb_2$

Cite as: Hai Zeng *et al*. 2026 *Chin. Phys. Lett.* **43** 070704

DOI CSTR

Recommended Articles

Magnetic Properties and Kondo Effect in Ce_3TiBi_5 under High Pressure

L.C. Fu *et al*.
Chin. Phys. Lett. **43**, 010705 (2026)

Emergent Fermi-Liquid-Like Phase by Melting a Holon Wigner Crystal in a Doped Mott Insulator on the Kagome Lattice

Xu-Yan Jia, Wen Huang, D. N. Sheng, and Shou-Shu Gong
Chin. Phys. Lett. **43**, 030706 (2026)

Finite Temperature Magnetism in the Triangular Lattice Antiferromagnet $KErTe_2$

Weiwei Liu, Zheng Zhang, Dayu Yan, Jianshu Li, Zhitao Zhang, Jianting Ji, Feng Jin, Youguo Shi, and Qingming Zhang
Chin. Phys. Lett. **41**, (2024)

InvDesFlow: An AI-Driven Materials Inverse Design Workflow to Explore Possible High-Temperature Superconductors

Xiao-Qi Han, Zhenfeng Ouyang, Peng-Jie Guo, Hao Sun, Ze-Feng Gao, and Zhong-Yi Lu
Chin. Phys. Lett. **42**, 047301 (2025)

Spin-Lattice Coupling Induced Rich Magnetic States in CrF_3 Monolayer

Fawei Zheng, and Yong Lu
Chin. Phys. Lett. **43**, 050714 (2026)

A series journal of Chinese Physical Society distributed by IOP Publishing

iopscience.iop.org/cpl | cpl.iphy.ac.cn

Chinese Physics Letters

Chin. Phys. Lett. **43** 070704 (2026)

LETTER

DOI: 10.1088/0256-307X/43/7/070704
CSTR: 32039.14.0256-307X.43.7.070704

Possible Inverse Magnetic Melting Effect in vdW-Like Kondo Lattice $CeSn_{0.75}Sb_2$

Hai Zeng(曾海)[1,*], Yiwei Chen(陈逸玮)[1], Zhuo Wang(王卓)[1], Shuo Zou(邹烁)[1], Kangjian Luo(罗康健)[1], Yang Yuan(袁洋)[1], Meng Zhang(张孟)[1], and Yongkang Luo(罗永康)[1,2,*]

[1]Wuhan National High Magnetic Field Center and School of Physics, Huazhong University of Science and Technology, Wuhan 430074, China
[2]State Key Laboratory of Advanced Electromagnetic Technology, Huazhong University of Science and Technology, Wuhan 430074, China

*Corresponding authors. Email: D202280149@hust.edu.cn; mpzslyk@gmail.com

Given the intimate connection between magnetic orders and the interplay among multiple degrees of freedom in heavy-fermion systems, controlling and understanding the associated inverse melting effect is crucial for unveiling novel condensed-matter states and their potential applications. Here, we report the growth of single-crystalline, quasi-two-dimensional van der Waals-like (vdW-like) Kondo lattice $CeSn_{0.75}Sb_2$ and its physical properties, determined by a combination of transport, magnetic, and thermodynamic measurements. We find that it hosts a fragile antiferromagnetic (AFM) order and a cluster-glass (CG) ground state, both of which are highly sensitive to external fields. Upon cooling under low in-plane magnetic fields, the AFM phase evolves into a polarized paramagnetic phase, either directly or indirectly through the intermediate CG phase. This process constitutes a possible inverse magnetic melting effect that restores the broken translational and rotational symmetries. Our work provides a rare paradigm of the inverse magnetic melting effect in vdW-like heavy-fermion materials and enriches the physics of conventional Kondo-lattice models.

Introduction

Inverse melting is a rare and intriguing phenomenon in which heating paradoxically stabilizes an ordered phase, in stark contrast to conventional thermal melting [1]. This counterintuitive phenomenon implies that the ordered phase hosts a higher entropy than the disordered state, a scenario resembling the so-called Pomeranchuk effect in liquid ^{3}He that has been widely exploited for cryogenic cooling [2]. Theoretical insights from spin models have elucidated the microscopic origin of this anomaly, attributing it to a significantly higher degeneracy of the interacting ordered states compared with the non-interacting ones, which can effectively reverse the standard energy–entropy competition [3,4]. In the realm of strongly correlated systems, it has been proposed that the competition between nearly degenerate magnetic states or intertwined orders may proliferate abundant low-energy excitations [5–10]. Such a scenario potentially endows an ordered phase with excess entropy relative to the disordered state, establishing the thermodynamic conditions required for inverse melting, as exemplified by twisted bilayer graphene [5–7], heavy-fermion metals [8–10], etc. In heavy-fermion systems, the competition between the Ruderman–Kittel–Kasuya–Yosida (RKKY) interaction and the Kondo effect [11], as well as the interplay among spin, orbital, and charge degrees of freedom [12–14], in principle, could create a manifold of nearly degenerate configurations as the source of extra entropy. Consequently, these systems exhibit immense potential for exploring the physics of inverse melting and may also inspire the design of functional quantum materials with electronic, magnetic, and cryogenic applications.

To realize inverse melting, it is necessary to drive the system by nonthermal tuning parameters such as magnetic field and hydrostatic pressure. A promising route for this is through the manipulation of spin dynamics in systems with high anisotropy. In this context, the intercalated $CeTmSb_2$ (Tm = transition metal) family offers an exceptional platform due to its remarkable structural tunability. Through substitution of the transition metal Tm, the lattice ratio $2\tilde{c}/(\tilde{a}+\tilde{b})$ varies between 2.07 and 2.65 [see more details in the Supplementary Materials (SM)], driving the system from a more three-dimensional magnetic exchange regime toward a two-dimensional (2D) limit [15–20]. Accompanying this modification in structural dimensionality, the crystal electric field (CEF) ground state alternates between a configuration dominated by $|\pm 5/2\rangle$ doublets (whose 4f spatial distribution is oblate, i.e., donut-shaped) and one characterized by $|\pm 1/2\rangle$ (dumbbell-shaped) [15,21,22]. This transformation directly reshapes the spatial distribution of the 4f orbitals and the magnetic anisotropy, thereby regulating the sign and direction of the RKKY interaction. According to an earlier simulation based on a mean-field model including two anisotropic RKKY interactions between nearest neighbors in the presence of tetragonal CEF, in-plane spin alignment (with $B_2^0 > 0$ and dominant $|\pm 1/2\rangle$ states) is favored in ferromagnetic (FM) compounds, whereas c-axis alignment ($B_2^0 < 0$ and dominant $|\pm 5/2\rangle$ states) is preferred in antiferromagnetic (AFM) compounds [15,18,20]. Here, B_2^0 is the CEF parameter of Stevens' operator $\hat{O}_2^0$. In other words, the structural dimensionality characterized by $2\tilde{c}/(\tilde{a}+\tilde{b})$ can place the magnetic ground state in a delicate energetic balance between AFM and FM orders. This competition may give rise to abundant low-energy fluctuations, which in turn establish the specific entropic landscape required for inverse melting.

Here, we report the successful synthesis of single-crystalline $CeSn_{0.75}Sb_2$ and a systematic investigation of its physical properties. At zero field, $CeSn_{0.75}Sb_2$ exhibits a fragile AFM order below ~7.5 K, followed by a transition into a cluster-glass (CG) state at around 2.7 K, characterized by the coexistence of FM clusters embedded within an AFM matrix. Applying a tiny magnetic field (less than 100 Oe) along the $\boldsymbol{a}$-axis is sufficient to align these clusters, whereas slightly higher fields (less than 0.2 T) drive the AFM order through a metamagnetic transition (MMT) into a polarized paramagnetic (PPM) state. A complete temperature–magnetic-field phase diagram of $CeSn_{0.75}Sb_2$ is mapped out, and a possible inverse magnetic melting effect is observed via transport, magnetic, and thermodynamic measurements. These results suggest a potential mechanism for applications in quantum switches, memory devices, or solid-state cryogens.

Received 6 April 2026; accepted 9 June 2026; published 7 July 2026
© 2026 Chinese Physical Society and IOP Publishing Ltd. All rights, including for text and data mining, AI training, and similar technologies, are reserved.

Check for updates

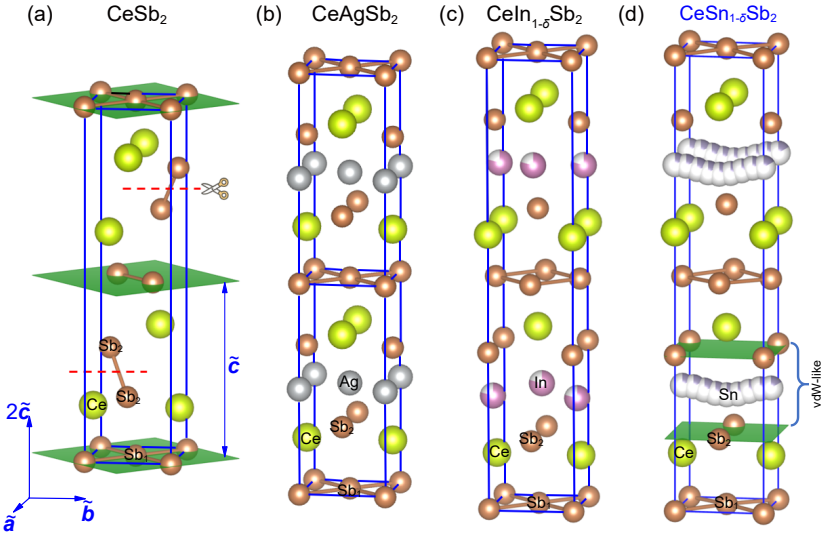

Fig. 1. Crystalline structures of the parent $CeSb_2$ and the intercalated $CeTmSb_2$ series. For a better comparison, the "unit" cell of $CeAgSb_2$ is doubled along $\tilde{\boldsymbol{c}}$, while those of $CeSb_2$ and $CeIn_{1-\delta}Sb_2$ are modified appropriately; see Fig. S1 of the SM for more details. Side views: (a) $CeSb_2$; (b) $CeAgSb_2$; (c) $CeIn_{0.8}Sb_2$; (d) $CeSn_{0.75}Sb_2$. For $CeSn_{0.75}Sb_2$, $\tilde{\boldsymbol{a}} = \boldsymbol{a}$, $\tilde{\boldsymbol{b}} = \boldsymbol{b}$, and $\tilde{\boldsymbol{c}} = \boldsymbol{c}/2$. $\tilde{c}$ characterizes the distance between adjacent Sb1 square nets (green squares), whereas $\tilde{a}$ and $\tilde{b}$ are the in-plane lattice parameters. The lattice parameters of these compounds are listed in Table S1 of the SM.

Experimental Details

Single crystals of $CeSn_{0.75}Sb_2$ were synthesized by the self-flux method. Ce flakes (99.9%), Sn granules (99.999%), and Sb grains (99.99%) were mixed in a molar ratio of 1 : 10 : 2.5, placed in an alumina crucible, and then sealed in a high-vacuum quartz tube. The mixture was heated to 950 ℃ over 24 h, held at that temperature for 12 h, and then slowly cooled to 500 ℃ at a rate of 2 ℃/h. The Sn flux was subsequently removed by centrifugation at this temperature. Flake-shaped $CeSn_{0.75}Sb_2$ single crystals were obtained, with a typical size of $3\times0.5\times0.02$ mm^3. The sample is stable in air. $LaSn_{0.75}Sb_2$ single crystals, the non-4f reference, were synthesized using a similar method. Energy-dispersive X-ray spectroscopy analysis confirmed the stoichiometric ratio of Ce, Sn, and Sb as 1.03(1) : 0.75(1) : 2.02(1). Phase purity and high crystalline quality were verified by X-ray diffraction using an XtaLAB mini II single-crystal diffractometer, where only the $[002l](l = 1,2,\ldots)$ peaks are visible (Fig. S2 of the SM).

Magnetic measurements, including both direct-current (DC) and alternating-current (AC) magnetization, were performed using a vibrating sample magnetometer (SQUID-VSM, Quantum Design). Zero-field specific heat measurements were performed using a commercial Physical Property Measurement System (PPMS-9, Quantum Design). Thermodynamic properties under an external magnetic field were characterized by AC calorimetry ($C_{\rm ac}$), which was measured using a differential Chromel-$Au_{99.93\%}Fe_{0.07\%}$ thermocouple to detect the heat–temperature response. Electrical resistivity measurements were carried out using a standard four-probe method with the applied magnetic field aligned along the $\boldsymbol{a}$ axis. Both AC calorimetry and electrical transport experiments were conducted in an Integra AC Mk II recondensing cryostat equipped with a 16 T superconducting magnet (Oxford Instruments).

Results and Discussion

The material we investigated here, $CeSn_{0.75}Sb_2$, belongs to the large family of $CeTmSb_2$ (Tm = intercalated metal) that can be viewed as Tm-intercalation into $CeSb_2$, as illustrated in Fig. 1. The parent compound $CeSb_2$ crystallizes in an orthorhombic structure with alternating layers of Sb1 square nets and Ce-Sb2 slabs stacked along the $\tilde{\boldsymbol{c}}$-axis [23]. The Tm intercalation takes place by breaking the chemical bonds between Sb2 atoms [cf. Fig. 1(a)]. Due to the new bonding between Tm and Sb2, the positions of Ce atoms are rearranged correspondingly, and this ultimately leads to various structural variants sharing the common chemical formula $CeTmSb_2$ (e.g., Tm = Ag, In, Sn, etc.) [24,25]. Among them, $CeSn_{0.75}Sb_2$ is special in that Sn atoms occupy three crystallographically distinct sites, each with a partial occupancy of approximately 20% [26], resulting in worm-like Sn chains along the $\tilde{\boldsymbol{b}}$-axis [Fig. 1(d)]. More strikingly, a previous Mössbauer spectroscopy study on polycrystalline samples revealed that the intercalated Sn atoms are essentially zero-valent, with negligible charge transfer [27]. This weakens the interlayer coupling, and indeed, the obtained $CeSn_{0.75}Sb_2$ single crystals exhibit van der Waals-like (vdW-like) behavior and can be easily exfoliated mechanically. A natural consequence of such intercalation is elongation of the $\tilde{\boldsymbol{c}}$-axis and increased structural anisotropy, as characterized by the enlarged ratio $2\tilde{c}/(\tilde{a}+\tilde{b}) \approx 2.65$ listed in Table S1 of the SM (the definitions of $\tilde{a}$, $\tilde{b}$ and $\tilde{c}$ are provided in Fig. S1 of the SM). This ratio significantly surpasses the critical AFM–FM boundary (≈ 2.37), placing the system deeply within the 2D regime, where the $|\pm 1/2\rangle$ doublet is expected to dominate the CEF ground state [15]. This extreme orbital dimensionality not only attenuates interlayer AFM coupling but also renders the magnetic ground state exceptionally susceptible to thermal and magnetic perturbations, potentially satisfying the conditions for inverse melting.

Figure 2(a) presents the temperature-dependent magnetic susceptibility $\chi(T)$ of $CeSn_{0.75}Sb_2$ single crystals under an external field of 0.1 T applied along different crystallographic axes. To compare with the earlier polycrystalline sample [27], the powder-averaged magnetic susceptibility [$\chi_{\rm avg} \equiv (\chi_a+\chi_b+\chi_c)/3$] is displayed in the inset. The Curie–Weiss law is well obeyed above 150 K, consistent with the literature. At low temperatures, χ_a, χ_b, and χ_c behave quite differently. To our surprise, a huge in-plane magnetic anisotropy is observed: at 1.8 K, χ_a is about 30 times larger than χ_b, whereas χ_b and χ_c are comparable. Isothermal field-dependent magnetization [$M(H)$] further confirms the $\boldsymbol{a}$-axis as the easy axis [see Fig. S3(b) of the SM]. Such giant in-plane anisotropy indicates an Ising-type magnetic character, a feature rarely reported in quasi-2D materials. Note that the lattice parameter b is only 6.6% larger than a (Table S1 of the SM). We speculate that the Sn chains aligned along the $\boldsymbol{b}$-axis probably play a key role in this in-plane anisotropic behavior. Since the magnetic anisotropy of Ce-based compounds is usually governed by the CEF effect, further investigations into the CEF-split 4f orbitals will be essential to clarify the origin of this unusual anisotropy. A kink is clearly seen in $\chi_a(T)$ near 7.5 K, followed by a rapid increase below 3 K, suggesting cascaded magnetic transitions in this compound, further

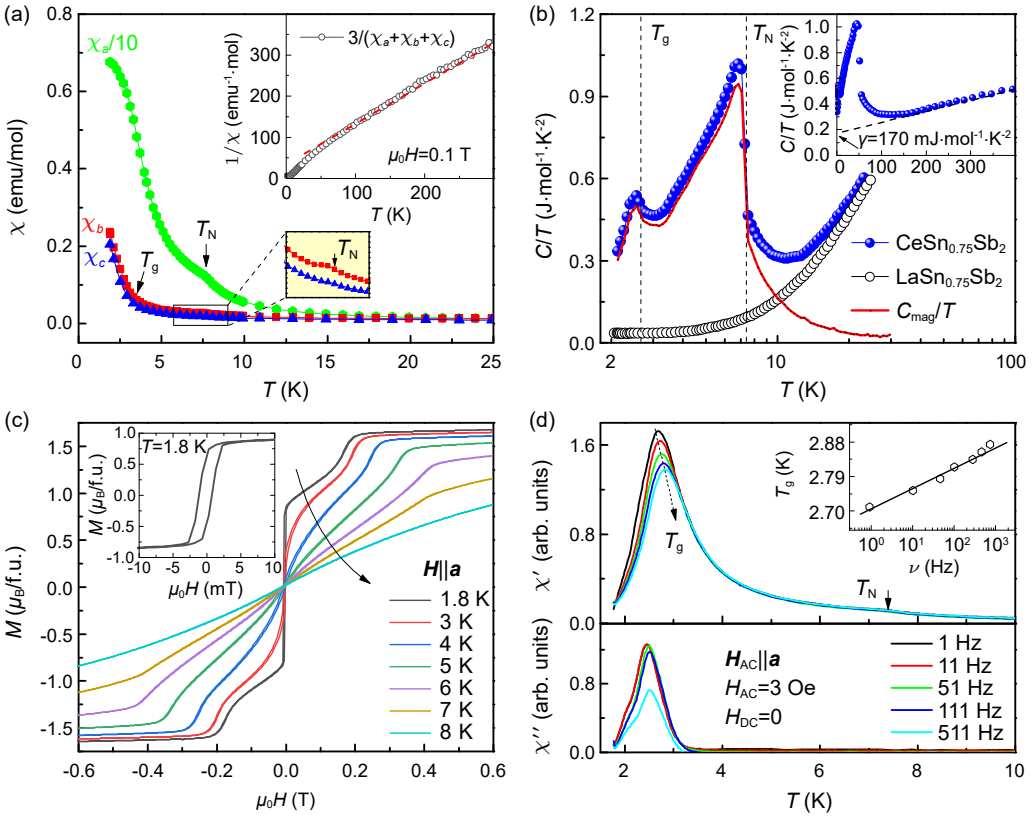

Fig. 2. (a) Temperature dependence of magnetic susceptibility χ for different field orientations measured with $\mu_0 H = 0.1$ T. The inset shows the temperature dependence of $1/\chi_{\rm avg}$, where $\chi_{\rm avg} = (\chi_a + \chi_b + \chi_c)/3$. The red dashed line is a fit to the Curie–Weiss law. (b) Specific heat C/T curves of $CeSn_{0.75}Sb_2$ and its nonmagnetic analog $LaSn_{0.75}Sb_2$. The red solid line represents the magnetic contribution $C_{\rm mag}/T$. The inset exhibits the C/T vs. T^2 plot whose intercept of the linear extrapolation yields the Sommerfeld coefficient $\gamma = 170$ mJ/mol·K^2. (c) Field dependence of the magnetization $M(H)$ at various temperatures for $\boldsymbol{H} \parallel \boldsymbol{a}$. The inset displays the magnetic hysteresis loop about zero field at 1.8 K. (d) Real (χ') and imaginary (χ'') parts of AC magnetic susceptibility vs temperature at different frequencies. The applied AC excitation field, $H_{\rm AC}$, was along $\boldsymbol{a}$. The inset shows T_g as a function of frequency ν.

supported by the specific heat data shown in Fig. 2(b). The critical temperatures of the two transitions are defined as $T_N = 7.5$ K and $T_g = 2.7$ K, respectively. Both transitions are discernible in $\chi_b(T)$, whereas T_N is hardly resolvable in $\chi_c(T)$. It is worth noting that an earlier study on polycrystalline $CeSn_{0.7}Sb_2$ revealed only a single transition near T_g [27]. All these observations suggest that the magnetic behavior is governed primarily by strong in-plane exchange interactions, with interlayer coupling remaining comparatively weak.

To further investigate the features of the two magnetic transitions, we carried out additional magnetization measurements at low temperature. The rapid increase of $\chi(T)$ below T_g is reminiscent of a FM-like correlation, and this seems to be supported by the bifurcation between zero-field-cooling and field-cooling protocols under small fields less than 80 Oe [cf. Fig. S3(a) of the SM], as well as the small hysteresis loop in isothermal magnetization $M(H)$ curves shown in Fig. 2(c). Such an irreversible behavior, however, may be also a typical signature of systems with frozen magnetic disorder, e.g., spin glasses or cluster glass [28–30], and superparamagnetic assemblies [31]. To further clarify this behavior, we measured the temperature dependence of AC susceptibility at multiple frequencies (ν) with fixed $\boldsymbol{a}$-axis excitation field $H_{\rm AC} = 3$ Oe [Fig. 2(d)]. The real part (χ') reveals two distinct features: a sharp peak near 2.7 K and a tiny hump around 7.5 K. The imaginary part (χ''), however, only uncovers the dissipation peak around 2.7 K. The absence of dissipation at T_N is consistent with the second-order nature of the AFM transition. More crucially, the peak near 2.7 K exhibits a pronounced frequency dependence [inset of Fig. 2(d)], a hallmark of spin-glass or CG dynamics. The corresponding Mydosh parameter [$\Phi = \Delta T_g/(T_g \Delta \log \nu)$] is determined to be ~0.023. This value is in better agreement with typical CG systems ($\Phi \sim 0.03$) than with canonical spin-glass systems ($\Phi \sim 0.005$) [32–34]. Therefore, the observed irreversibility in the susceptibility curves is more likely a consequence of the CG state, wherein randomly frozen FM clusters are embedded inside a disordered AFM matrix, and different cooling paths can lead to distinct cluster orientations. This configuration probably originates from the local crystalline disorder induced by the partial occupancy of Sn at three independent sites. Unlike canonical metallic spin glasses where random placement of magnetic moments generates sign-oscillating RKKY interactions, the chemical disorder alters the local ligand environment around Ce ions, which theoretically could lead to a spatial modulation of the hybridization between Ce 4f and conduction electrons. Such hybridization fluctuations may interact with the randomness in RKKY exchange, promoting the formation of a CG state. A similar mechanism has been established in other heavy-fermion systems, such as $CePd_{1-x}Rh_x$ [35] and URh_2Ge_2 [36], where mixed occupation of ligand sites produces a broad distribution of local Kondo temperatures.

The magnetic transitions in $CeSn_{0.75}Sb_2$ are also seen in electrical transport properties, as shown in Fig. 3. For comparison, the non-4f counterpart $LaSn_{0.75}Sb_2$ is also shown in the same frame. $LaSn_{0.75}Sb_2$ behaves as a simple metal: ρ decreases almost linearly with decreasing T above 100 K, and then crosses over into Fermi-liquid behavior [$\rho \propto T^2$, cf. the dashed line in Fig. 3(a)] at low temperature. $CeSn_{0.75}Sb_2$ also shows a metallic profile, but additional anomalies are observable. First, a broad hump is seen around 120 K, which can be more clearly identified by subtracting the resistivity of $LaSn_{0.75}Sb_2$ [cf. $\rho_{\rm mag}$ shown in the inset to Fig. 3(a)]. Such a broad peak in $\rho_{\rm mag}(T)$ is commonly seen in Ce-based compounds and should be ascribed to scattering between thermally populated CEF levels [37,38]. Further decreasing temperature to below 50 K, as incoherent Kondo scattering sets in, the resistivity turns up and increases logarithmically until a second broad peak centered at about 10 K is observed. This implies

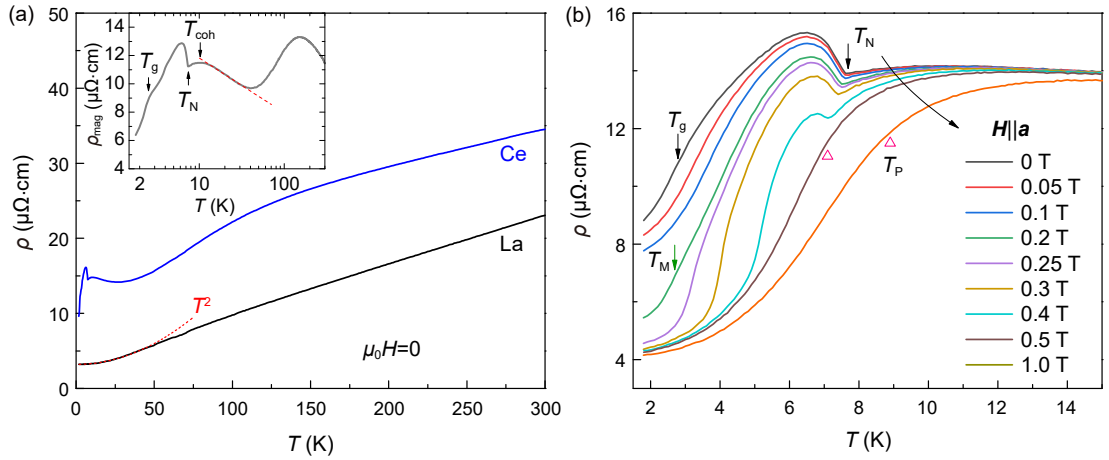

Fig. 3. Longitudinal resistivity of $CeSn_{0.75}Sb_2$. (a) $\rho(T)$ profile of $CeSn_{0.75}Sb_2$ as compared with that of $LaSn_{0.75}Sb_2$. The inset displays the contribution of the 4f-electrons to the resistivity, revealing the coherent Kondo scale T_{coh}, and the two magnetic transitions at T_N and T_g. (b) The temperature dependence of the resistivity under various magnetic fields with $\boldsymbol{H} \parallel \boldsymbol{a}$ and $\boldsymbol{I} \parallel \boldsymbol{a}$. The open triangles signify the characteristic temperature T_P.

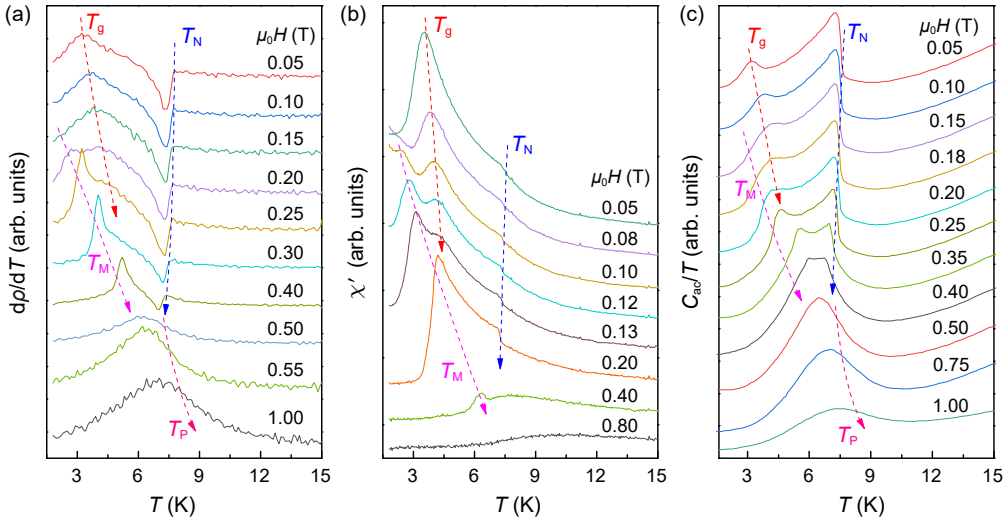

Fig. 4. Temperature dependence of (a) $d\rho/dT$, (b) χ', and (c) C_{ac}/T. For all these measurements, both H_{DC} and H_{AC} were applied along $\boldsymbol{a}$. The AC susceptibility was measured with an excitation amplitude of 3.8 Oe at a frequency of 511 Hz, while the AC specific heat was recorded with a modulation frequency of 51 Hz. The curves are shifted vertically for clarity. T_N (blue arrows), T_g (red arrows), and T_M (pink arrows) denote the AFM, CG, and MMT temperatures, respectively.

the establishment of Kondo coherence and yields an important temperature scale for Kondo lattices, $T_{coh} \approx 10$ K. Around T_N, resistivity increases sharply, passes through a peak, and then decreases rapidly. Such a $\rho(T)$ profile near the AFM transition is generally attributed to competition between suppressed spin-scattering rates and reduced carrier concentration resulting from gap opening on the Fermi surface upon AFM ordering. In fact, the reduction of carrier density is also supported by the Hall effect, as shown in Fig. S4 of the SM. One possibility is that this magnetic transition is also accompanied by a density-wave order, which deserves further investigation. A distinct kink is observed near 2.7 K ($\sim T_g$), corresponding to the low-temperature magnetic cluster transition. As shown in Fig. 3(b), application of a magnetic field initially suppresses T_N, and the sharp resistivity change near T_N becomes progressively smeared out. For fields larger than 0.5 T, no anomaly in resistivity is observed in this region; instead, $\rho(T)$ decreases smoothly and rapidly. This indicates that the magnetic moments tend to be polarized by the external field prior to undergoing the AFM transition, significantly reducing spin scattering. Similar behavior was also reported in CeAlGe [10]. A new characteristic temperature T_P is thus defined to describe the polarization of Ce moments under field. Interestingly, when the field exceeds 0.2 T, an additional magnetic transition emerges at $T_M \sim 2.65$ K. Both T_g and T_M increase with magnetic field, which can be better seen in $d\rho/dT$ [Fig. 4(a)] and will be discussed below.

We now turn back to the isothermal magnetization results of $CeSn_{0.75}Sb_2$. Another prominent feature of the $M(H)$ curves is that they show slope changes along different crystallographic directions at 1.8 K, as shown in Fig. S3(b) of the SM. In particular, for field along $\boldsymbol{a}$, a field-induced MMT is clearly seen near 0.17 T [Fig. 2(c)]. Above this critical field, the magnetization levels off. The saturated moment reaches 1.68 μ_B/f.u. Unexpectedly, as temperature increases, the critical field for this MMT shifts to higher values; meanwhile, the signature of the MMT gradually fades and becomes indistinguishable above T_N. First, the observation of this field-induced MMT affirms that the ground state of $CeSn_{0.75}Sb_2$ in the temperature range $T_g < T < T_N$ is antiferromagnetically ordered, albeit the exact magnetic structure awaits determination by complementary techniques such as neutron scattering. Second, the upward shift of the critical field with increasing temperature is unusual: it directly implies that reorientation of the magnetic moments becomes increasingly difficult at elevated temperatures. Such behavior is counter-intuitive and reminds us of the possibility that an inverse melting of the magnetic ordering may take place in this system.

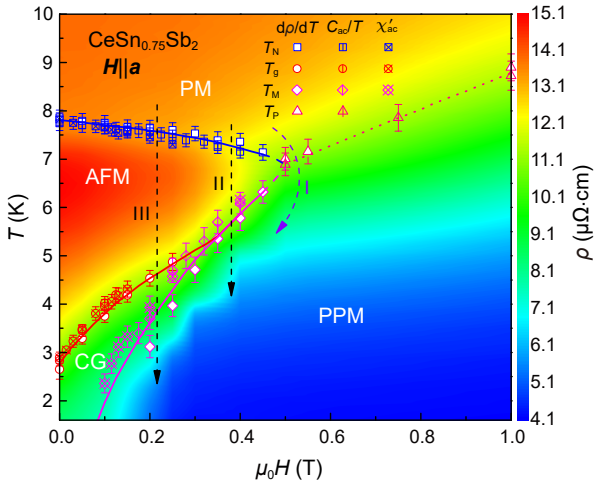

Fig. 5. False-color phase diagram of $CeSn_{0.75}Sb_2$ constructed from a contour plot of $\rho(\mu_0 H, T)$, with the field applied along the $\boldsymbol{a}$-axis. The abbreviations are: AFM (antiferromagnetic), PM (paramagnetic), FP (field-polarized), CG (cluster glass). The dashed arrows I–III represent different thermodynamic cooling paths from PM to PPM under variable magnetic fields. The yellow dashed line denotes the crossover from PM to field-induced PPM state. Note that cooling destabilizes the ordered state even without field or passing through the CG phase.

In order to gain deeper insights into the inverse melting phenomenon, systematic measurements of resistivity ($d\rho/dT$), the real part of the AC magnetic susceptibility (χ'), and AC calorimetry (C_{ac}/T)* were conducted on $CeSn_{0.75}Sb_2$ with the magnetic field applied along the $\boldsymbol{a}$-axis; the results are displayed in Fig. 4. T_N shifts weakly to lower temperatures with increasing magnetic field, which is consistent with AFM order. In contrast, the evolution of T_g with field is opposite to that of T_N. When the magnetic field exceeds ~0.1 T, both $d\rho/dT$ and χ' exhibit a distinct peak near T_M associated with the MMT, whereas C_{ac}/T displays only a broad shoulder. T_M increases with field faster than T_g, and the two merge when the field exceeds ~0.2 T, reforming a sharp peak. As the magnetic field is further increased, the Ce moments tend to be polarized, and therefore T_N, T_g, and T_M are no longer distinguishable. In general, the three measurements consistently characterize the magnetic transitions. Under identical magnetic fields (e.g., 0.1 T, 0.2 T, and 0.4 T), the T_N values determined by different techniques are in good agreement, whereas T_g and T_M display measurable variations. This is probably related to the glassy dynamics in the CG state, whose relaxation time spectrum leads to a frequency dependence of the freezing temperatures.

Based on the results described above, a temperature–field phase diagram of $CeSn_{0.75}Sb_2$ for $\boldsymbol{H} \parallel \boldsymbol{a}$ is constructed in Fig. 5, where the false color indicates the magnitude of $\rho(\mu_0 H, T)$. Upon cooling in zero field, the system successively enters the AFM state below T_N and the CG phase below T_g. Applying an external magnetic field polarizes the magnetic phases (AFM and CG) into a PPM state, with the transition boundary determined by T_M. The T_N and T_M boundaries intersect at approximately (0.5 T, 6.9 K). This diagram reveals three distinct cooling pathways depending on the strength of the applied magnetic field: (i) For fields above ~0.5 T, the system exhibits a smooth crossover from the paramagnetic state to the PPM state, with no distinct phase transition (Path I). Since the applied magnetic field explicitly breaks time-reversal symmetry, no additional **spontaneous** symmetry breaking occurs between PM and PPM, and a phase transition is avoided. (ii) When cooled in a moderate field, the system undergoes a PM-to-AFM transition followed by the formation of the PPM state (Path II). Since the broken translational and rotational symmetries in the high-T AFM phase are restored in the low-T PPM phase, this process is identified as inverse melting [3,4,9]. (iii) In the low-field regime (Path III), inverse melting also takes place upon cooling, passing through an intermediate CG phase. It is crucial to emphasize that the observed inverse magnetic melting is not a trivial consequence of field-induced polarization. If the AFM state is solely suppressed by Zeeman effect, one would anticipate a monotonic suppression of the ordered phase. However, the observed reentrant restoration of the higher-symmetry phase upon field-cooling is inconsistent with this scenario, indicating a mechanism beyond energy-driven.

The inverse melting effect has been observed in a variety of condensed-matter systems and is generally explained as a consequence of the energy–entropy competition. Besides the classic Pomeranchuk effect in liquid ^{3}He, a recent example is the twisted bilayer graphene [5,6], in which the electronic state "freezes" upon heating, from a metallic phase (wherein electrons move freely) to a nearly insulating phase (in which the electrons are localized and "ordered"). The latter is favored at elevated temperatures due to greater entropy gain arising from the cooperative behavior of isospin degrees of freedom [39]. In spin systems, magnetic orders usually get further stabilized as temperature approaches zero, owing to the quench of thermal fluctuations. In the presence of a magnetic field, the Zeeman energy competes with magnetic exchange interactions, and the AFM order is often suppressed and terminated by either a quantum critical point or first-order quantum phase transition [40–43]. In contrast, the occurrence of inverse melting is much rarer. While the exact reason for the inverse magnetic melting effect in $CeSn_{0.75}Sb_2$ is to be understood, one possibility is that the emergence of the CG state out of the AFM order is associated with an enhanced degeneracy of magnetic configurations, which may facilitate entropy-driven inverse melting behavior. Altogether, the AFM order manifests itself as an entropy-driven metastable phase that is confined to a finite temperature window and collapses upon cooling. Additional evidence supporting the entropy-driven mechanism can be provided by the magneto-calorimetric measurements shown in Fig. S6 of the SM. These findings highlight the potential of utilizing entropy as a tuning parameter.

Finally, it is necessary to revisit the specific heat results in Fig. 2(b). A C/T vs. T^2 plot yields the Sommerfeld coefficient $\gamma = 170$ mJ/mol·K^2. By integrating C_{mag}/T with respect to T, we derive the magnetic entropy as a function of temperature, as shown in Fig. S5 of the SM, where C_{mag} is the 4f magnetic contribution to the specific heat. The Kondo scale (T_K) can thus be estimated from $S_{mag}(T_K/2) = 0.4R\ln 2$ [12], which results in $T_K \approx 10$ K. All these results indicate that $CeSn_{0.75}Sb_2$ is a moderately heavy-fermion metal with relatively weak Kondo effect, sitting in the magnetically-ordered regime of the Doniach phase diagram [11]. It is noteworthy that inverse magnetic melting effect has so far been reported in several Ce-based heavy-fermion materials, including Ce_3TiSb_5 [44] and CeAlGe [10]. In both Ce_3TiSb_5 and CeAlGe, the AFM transitions are initially enhanced under pressure [10,45], and the same holds for $CeSn_{0.75}Sb_2$. (The pressure effect of $CeSn_{0.75}Sb_2$ will be published separately). These commonalities tend to suggest that inverse magnetic melting effect in heavy-fermion systems is more favored in those with weak Kondo coupling. The underlying mechanism for this calls for more investigations, both experimentally and theoretically.

Conclusion

In summary, the vdW-like Kondo lattice $CeSn_{0.75}Sb_2$ exhibits a variety of magnetic phases that are highly sensitive to magnetic fields, alongside a rare and highly tunable inverse melting effect. At zero field, the system hosts a fragile AFM order and a CG ground state, which are readily suppressed by an applied in-plane magnetic field. Notably, multi-pathway inverse melting occurs upon cooling at

*Since $CeSn_{0.75}Sb_2$ single crystals are very thin, typically ~20 μm, and specific-heat measurements under an in-plane magnetic field is very difficult in PPMS, we performed AC calorimetry measurement instead.

specific magnetic fields. The microscopic origin of the inverse magnetic melting behavior remains elusive but likely arises from a thermodynamic preference for a high-entropy ordered phase. These findings not only extend the material basis of quasi-2D heavy-fermion compounds beyond $CeTe_3$ [46] and the recently discovered CeSiI [47], but also offer a fresh thermodynamic perspective for understanding the complex phases in correlated electronic systems.

Acknowledgements

The authors thank Zhentao Wang, Xiaoxiao Zhang, and Yifeng Yang for helpful discussions. This work was supported by the National Key R&D Program of China (Grant Nos. 2022YFA1602602 and 2023YFA1609600), the National Natural Science Foundation of China (Grant Nos. U23A20580 and 52588101), and Beijing National Laboratory for Condensed Matter Physics (Grant No. 2024BNLCMP-KF004).

References

[1] Tammann G 1925 *The States of Aggregation: The Changes in the State of Matter in Their Dependence Upon Pressure and Temperature* (New York: Van Nostrand)
[2] Richardson R C 1997 *Rev. Mod. Phys.* **69** 683
[3] Schupper N and Shnerb N M 2004 *Phys. Rev. Lett.* **93** 037202
[4] Schupper N and Shnerb N M 2005 *Phys. Rev. E* **72** 046107
[5] Rozen A, Park J M, Zondiner U, Cao Y, Rodan-Legrain D, Taniguchi T, Watanabe K, Oreg Y, Stern A, Berg E, Jarillo-Herrero P, and Ilani S 2021 *Nature* **592** 214
[6] Saito Y, Yang F, Ge J, Liu X, Taniguchi T, Watanabe K, Li J I A, Berg E, and Young A F 2021 *Nature* **592** 220
[7] Zhang M, Zhao X, Watanabe K, Taniguchi T, Zhu Z, Wu F, Li Y, and Xu Y 2022 *Phys. Rev. X* **12** 041015
[8] Continentino M A and Ferreira A S 2004 *Phys. Rev. B* **69** 233104
[9] Ye H Q, Zhang Y N, Le T, Yuan H Q, and Smidman M 2024 *Phys. Rev. B* **109** 104414
[10] He X, Li Y, Zeng H, Zhu Z, Tan S, Zhang Y, Cao C, and Luo Y 2023 *Sci. China Phys. Mech. Astron.* **66** 237011
[11] Doniach S 1977 *Physica B+C* **91** 231
[12] Gegenwart P, Si Q, and Steglich F 2008 *Nat. Phys.* **4** 186
[13] Tsujimoto M, Matsumoto Y, Tomita T, Sakai A, and Nakatsuji S 2014 *Phys. Rev. Lett.* **113** 267001
[14] Kobayashi H, Sakaguchi Y, Kitagawa H, Oura M, Ikeda S, Kuga K, Suzuki S, Nakatsuji S, Masuda R, Kobayashi Y, Seto M, Yoda Y, Tamasaku K, Komijani Y, Chandra P, and Coleman P 2023 *Science* **379** 908
[15] Rosa P F S, Bourg R J, Jesus C B R, Pagliuso P G, and Fisk Z 2015 *Phys. Rev. B* **92** 134421
[16] Thamizhavel A, Takeuchi T, Okubo T, Yamada M, Asai R, Kirita S, Galatanu A, Yamamoto E, Ebihara T, Inada Y, Settai R, and Onuki Y 2003 *Phys. Rev. B* **68** 054427
[17] Seo S, Wang X, Thomas S M, Rahn M C, Carmo D, Ronning F, Bauer E D, dos Reis R D, Janoschek M, Thompson J D, Fernandes R M, and Rosa P F S 2020 *Phys. Rev. X* **10** 011035
[18] Jang J, Yi C, and Rhee J Y 2024 *Phys. Rev. B* **109** 054431
[19] Muro Y, Takeda N, and Ishikawa M 1997 *J. Alloys Compd.* **257** 23
[20] Park T, Sidorov V A, Lee H, Fisk Z, and Thompson J D 2005 *Phys. Rev. B* **72** 060410
[21] Willers T, Strigari F, Hu Z, Sessi V, Brookes N B, Bauer E D, Sarrao J L, Thompson J D, Tanaka A, Wirth S, Tjeng L H, and Severing A 2015 *Proc. Natl. Acad. Sci. USA* **112** 2384
[22] Cheng K, Wang L, Xu Y, Yang F, Zhu H, Ke J, Lu X, Xia Z, Wang J, Shi Y, Yang Y, and Luo Y 2019 *Phys. Rev. Mater.* **3** 021402
[23] Wang R and Steinfink H 1967 *Inorg. Chem.* **9** 1685
[24] Ferguson M J, Ellenwood R E, and Mar A 1999 *Inorg. Chem.* **38** 4503
[25] Araki S, Metoki N, Galatanu A, Yamamoto E, Thamizhavel A, and Onuki Y 2003 *Phys. Rev. B* **68** 024408
[26] Ferguson M J, Hushagen R W, and Mar A 1996 *Inorg. Chem.* **35** 4505
[27] Deakin L, Ferguson M J, Sprague M J, Mart A, Sharma R D, and Jones C H W 2002 *J. Solid State Chem.* **164** 292
[28] Binder K and Young A P 1986 *Rev. Mod. Phys.* **58** 801
[29] Wu J and Leighton C 2003 *Phys. Rev. B* **67** 174408
[30] Luo Y, Cao C, Si B, Li Y, Bao J, Guo H, Yang X, Shen C, Feng C, Dai J, Cao G, and Xu Z A 2013 *Phys. Rev. B* **87** 161121
[31] Bedanta S and Kleemann W 2009 *J. Phys. D: Appl. Phys.* **42** 013001
[32] Mydosh J A 2015 *Rep. Prog. Phys.* **78** 052501
[33] Xiao X, Zhao X, Guo J, Liu W, and Zhang Z 2020 *J. Alloys Compd.* **816** 152678
[34] Bag P, Baral P R, and Nath R 2018 *Phys. Rev. B* **98** 144436
[35] Westerkamp T, Deppe M, Küchler R, Brando M, Geibel C, Gegenwart P, Pikul A P, and Steglich F 2009 *Phys. Rev. Lett.* **102** 206404
[36] Süllow S, Nieuwenhuys G J, Menovsky A A, Mydosh J A, Mentink S A M, Mason T E, and Buyers W J L 1997 *Phys. Rev. Lett.* **78** 354
[37] Bauer E and Rotter M 2010 *Properties and Applications of Complex Intermetallics*, Book series on Complex Metallic Alloys, edited by Ester Belin-Ferre (Singapore: World Scientific Publishing) p. 183
[38] Luo Y, Bao J, Shen C, Han J, Yang X, Lv C, Li Y, Jiao W, Si B, Feng C, Dai J, Cao G, and Xu Z A 2012 *Phys. Rev. B* **86** 245130
[39] Lian B 2021 *Nature* **592** 191
[40] Grigera S A, Perry R S, Schofield A J, Chiao M, Julian S R, Lonzarich G G, Ikeda S I, Maeno Y, Millis A J, and Mackenzie A P 2001 *Science* **294** 329
[41] Gegenwart P, Custers J, Geibel C, Neumaier K, Tayama T, Tenya K, Trovarelli O, and Steglich F 2002 *Phys. Rev. Lett.* **89** 056402
[42] Luo Y, Ronning F, Wakeham N, Lu X, Park T, Xu Z A, and Thompson J D 2015 *Proc. Natl. Acad. Sci. USA* **112** 13520
[43] Jiao L, Chen Y, Kohama Y, Graf D, Bauer E D, Singleton J, Zhu J X, Weng Z, Pang G, Shang T, Zhang J, Lee H O, Park T, Jaime M, Thompson J D, Steglich F, Si Q, and Yuan H Q 2015 *Proc. Natl. Acad. Sci. USA* **112** 673
[44] Jackson D E, Stevenson T, Jones B *et al.* 2019 *Complex Phase Diagram and Reentrant Disorder in Ce_3TiSb_5.* https://nationalmaglab.org/user-facilities/high-b-t/research/science-highlights/complex-phase-diagram-ce3tisb5/
[45] Shinozaki M, Motoyama G, Nishigori S, Yamaguchi A, Yamane Y, Mutou T, Fujiwara K, Manago M, Miyoshi K, and Sumiyama A 2022 *J. Phys.: Conf. Ser.* **2164** 012040
[46] Zeng H, Zhang Y, Ji B, Cai J, Zou S, Wang Z, Dong C, Luo K, Yuan Y, Wang K, Zhang J, Xi C, Wang J, Li L, Dai Y, Li J, and Luo Y 2026 *Newton* **2** 100320
[47] Posey V A, Turkel S, Rezaee M *et al.* 2024 *Nature* **625** 483